Laser-Accelerated Ions from a Shock-Compressed Gas Foil

M. H. Helle,[1,*] D. F. Gordon,[1] D. Kaganovich,[1] Y. Chen,[2,†] J. P. Palastro,[1] and A. Ting[2]
[1]*Plasma Physics Division, Naval Research Laboratory, Washington, D.C. 20375, USA*
[2]*Research Support Instruments, Lanham, Maryland 20706, USA*

(Received 14 March 2016; revised manuscript received 22 June 2016; published 10 October 2016)

We present results of energetic laser-ion acceleration from a tailored, near solid density gas target. Colliding hydrodynamic shocks compress a pure hydrogen gas jet into a 70 μm thick target prior to the arrival of the ultraintense laser pulse. A density scan reveals the transition from a regime characterized by a wide angle, low-energy beam (target normal sheath acceleration) to one of a more focused beam with a high-energy halo (magnetic vortex acceleration). In the latter case, three-dimensional simulations show the formation of a *Z* pinch driven by the axial current resulting from laser wakefield accelerated electrons. Ions at the rear of the target are then accelerated by a combination of space charge fields from accelerated electrons and Coulombic repulsion as the pinch dissipates.

DOI: 10.1103/PhysRevLett.117.165001

High-energy ions have been accelerated by means of laser interactions with overdense or tenuous plasmas for over a decade [1,2]. These investigations relied on varying accelerating mechanisms, the most prominent being laser hole boring [3], target normal sheath acceleration (TNSA) [4], laser blowout acceleration [5], and radiation pressure acceleration [6]. All of these mechanisms primarily rely on accelerating fields produced by charge separation between the massive ions and laser-accelerated hot electrons. While progress continues to be made, these experiments have relied on solid targets that can limit repetition rate and purity of the accelerated ions.

Recently long-wave infrared laser acceleration of ions by means of electrostatic shock acceleration in gas targets has become a reality [7,8]. These experiments take advantage of short pulse CO_2 lasers ($\lambda_0 = 10.6\ \mu$m) that have a critical plasma density within the operational range of gas jets (10^{18}–10^{20} cm^{-3}), where the critical density $[n_{\mathrm{crit}} = (2\pi c)^2 m_e \epsilon_0 / e^2 \lambda_0^2]$ is the cutoff density at which electromagnetic waves no longer propagate within the plasma.

While this type of acceleration technique may be difficult to achieve for ultrashort pulse near-infrared lasers since it requires strong electron heating, the advantages of gas targets remain; namely, they are relatively simple, produce high purity targets with variable densities, and can be operated at high repetition rates. Unfortunately, current gas jets produce densities well below the critical density for near-infrared wavelengths, where most of the world's terawatt and petawatt lasers operate.

In this Letter, we report the acceleration of protons from a new type of target, a "gas foil," that has been developed at the Naval Research Laboratory (NRL) [9,10]. The target is based on the propagation of strong hydrodynamic shocks in gas. The shock front acts to increase the local density to values near critical density for near-infrared wavelengths ($\sim 10^{21}$ cm^{-3}) and steepen the density gradients. Gradients at both the front and rear of the target are important in that they reduce deleterious laser propagation effects, including ionization defocusing and filamentation, while at the same time aiding the production of energetic particles as they are accelerated out of the rear of the target. Additionally, the target can be operated at various densities and at high repetition rates. In previous work [11], it was observed that the gas flow returns to its preshocked state in $\sim\mu$s. Thus, repetition rates in excess of 10 kHz are possible. Here, we will present results of $\sim$2 MeV proton acceleration from this target using only 500 mJ of laser energy, as well as a discussion of the relevant mechanisms, including TNSA and magnetic vortex acceleration.

Magnetic vortex acceleration is a recently proposed and as of yet experimentally unconfirmed acceleration technique that exhibits a myriad of physical processes [9,12–16]. In particular, this scheme relies on large magnetic field gradients produced at a plasma gradient to drive acceleration, Fig. 1. Using a gas foil target to access this mechanism provides a route to generate high-energy ions at high repetition from a high purity source that leverages compact solid-state lasers.

The experimental setup is shown in Fig. 2. Strong hydrodynamic shock waves are ignited in a standard gas jet in vacuum using nanosecond frequency doubled Nd:YAG pulses. The individual shocks produce a profile that consists of a sharp leading edge, followed by a slow falling edge, with a peak value that is $(\gamma + 1)/(\gamma - 1)$, where γ is the ratio of specific heat. This value can range from 4 to 10 dependent on the degree of excitation of the internal degrees of freedom of the gas. When two shocks are allowed to collide, the resulting peak density is the sum of the individual shock densities. This technique provides the density increase necessary to approach critical density. For these acceleration experiments two blast waves were used to tailor the hydrogen gas flow

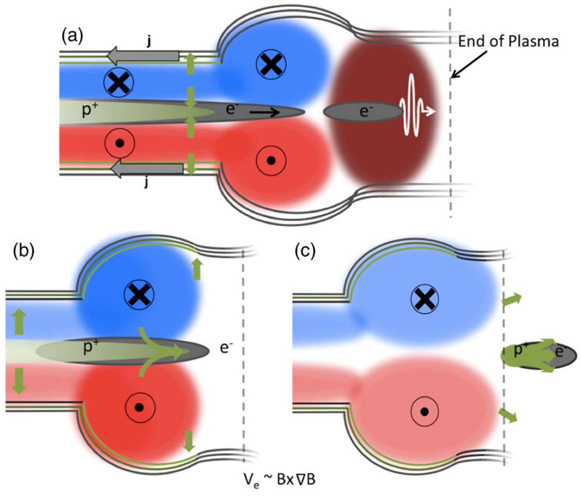

FIG. 1. Illustration of the acceleration process. (a) An intense laser pulse drives a self-modulated wakefield, injecting and accelerating a high-energy electron beam from the ambient plasma. A *Z* pinch of the trailing electrons and ions is driven by the high current beam. (b) The large magnitude and gradient of the magnetic field leads to an axial guiding center drift for a secondary electron beam moving out of the plasma. (c) The space-charge fields of the exiting electrons accelerate ambient plasma ions. The *Z*-pinched compressed ions explode out radially, while cold ions collectively escape with the electron beam.

into a 75 μm thick gas "foil" with 30 μm gradients and tunable peak densities from $(2.5–5) \times 10^{20}$ molecules cm^{-3}. This provides a pure hydrogen target at densities and gradients previously unexplored. The formation of the target is monitored using a 400 nm, 50 fs laser probe that goes to shadowgraphic and interferometric diagnostics (see Supplemental Material [17]).

The interaction is driven by a 500 mJ, 800 nm, 50 fs laser pulse generated by the Ti:Sapphire Femtosecond Laser system at NRL. The pulse is focused, using an $f/2$ off-axis parabola, to a vacuum spot size of 2.6 μm, $1/e^2$, reaching a peak intensity of 1×10^{20} W cm^{-2}. We focused the laser pulse at the front edge of the foil to allow it to relativistically self-focus within the density ramp. This allows the pulse to reach higher intensities. The energy and spatial distribution of the ions is measured using a 1 mm thick CR-39 plate with aluminum filters of varying thickness spaced perpendicular to the laser polarization axis. The stack was placed 13 cm from the gas jet to prevent laser damage of the plate and to cover a solid angle of 0.25 sr.

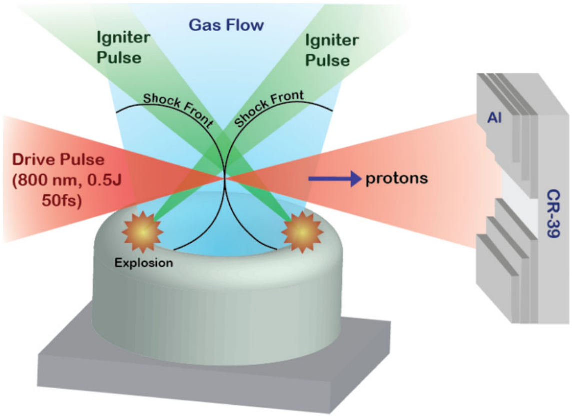

FIG. 2. A schematic of the experimental setup including the CR-39 detector stack. A 1 mm supersonic gas jet delivers the neutral gas while laser ignited strong hydrodynamic shocks act to shape it. The accelerated ions are then detected by CR-39 plates with varying Al filters.

A density scan was performed over the operational range of our gas jet at intervals of 0.5×10^{20} molecules cm^{-3}. Assuming fully ionized hydrogen, this corresponds to peak plasma densities of $n_e = (0.3–0.6)n_{\mathrm{crit}}$. It was observed that at densities above $0.4n_{\mathrm{crit}}$, a proton beam contained within the length of detector was accelerated in the forward direction, though outside the laser vacuum spot size and 15° from its axis. The beam was unable to penetrate even a single filter layer (9 μm) and, thus, had peak energy of < 700 keV. Upon closer examination of the tracks produced, the pit diameters were < 10 μm, corresponding to the proton energies < 200 keV [18]. An example detector image is given in Fig. 3.

At a density of $0.3n_{\mathrm{crit}}$, we observed protons penetrating through the 9, 18, and 27 μm thick filters with no proton penetrating the 36 μm thick filter (Fig. 3). This indicates a broad energy distribution of protons with a maximum energy between 1.5 and 1.9 MeV. Unlike the higher-density cases, the spatial distribution of the protons within the unshielded region extends beyond the length of the detector. It is characterized by an intense beam near the vacuum laser axis (left boundary) with a highly nonuniform distribution to the right of that. These nonuniformities are consistent with the distribution of higher-energy protons observed in the shielded regions above and below.

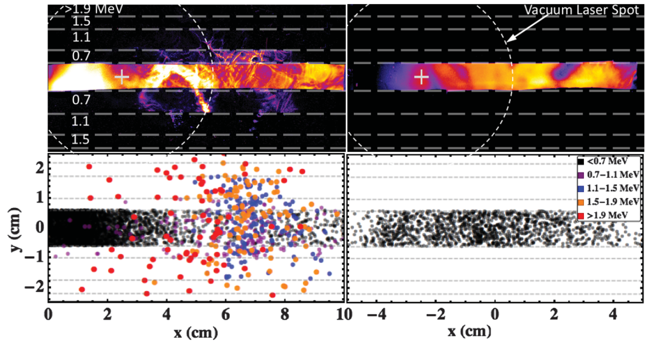

FIG. 3. False-color image of 10×5 cm^2 CR-39 plates for the cases of $0.3n_{\mathrm{crit}}$ (left) and $0.6n_{\mathrm{crit}}$ (right). The detector covers a solid angle of 0.25 sr. The laser axis and vacuum spot size are included on both. Dashed horizontal lines represent the location of the filters and their lower-energy bound is listed on the left. On the bottom are plots of simulated test particles projected to the plane of the detector color coded to the experimental energy buckets. See Fig. 4 for contour plots of the simulated proton distribution.

The origin of these accelerated protons was investigated using the TurboWAVE 3D particle-in-cell code (PIC) [19]. The simulation box is $78 \times 78 \times 260\ \mu\mathrm{m}^3$ with a grid spacing of $\Delta x = \Delta y = \lambda_0/2.5$ and $\Delta z = \lambda_0/12$. It was as initialized using the experimental parameters and density profiles (see Supplemental Material [17]). Test particles were placed within the simulation box, their orbits were tracked and projected to the detector plane. The projected ion test particles for the cases of $0.3n_{\mathrm{crit}}$ and $0.6n_{\mathrm{crit}}$ are given in Figs. 3 and 4. In Fig. 3 the test particle spatial distributions are filtered by energy to match the experimental conditions, and show excellent agreement. To understand the underlying process, the full simulated distribution with the corresponding proton density profiles are given in Fig. 4. For the $0.6n_{\mathrm{crit}}$ case, the protons are contained within a beam width of 8 cm FWHM and have a peak energy of 140 keV, consistent with the experimental track diameters. Examining the results of the PIC simulation, we see that the laser pulse is unable to penetrate the target, Fig. 4. The protons that are accelerated in the forward direction originate from the rear side of the target. They are accelerated by space-charge fields produced from hot electrons generated by the laser-target interaction exiting the rear of the target. This is consistent with the TNSA mechanism [4]. We also note that the proton beam is shifted by 3.5 cm (15°) from the laser axis. We believe that this is a direct consequence of the colliding spherical shocks. When the hot electrons exit the plasma, they accelerate the protons normal to the exit surface. Since the exit is defined by a short radius, concave surface, any slight misalignment between the laser axis and the origin of the shock would result in a significant shift in the proton beam axis.

Examining the $0.3n_{\mathrm{crit}}$ case, we see a vastly different situation. The forward accelerated protons are characterized by a low-energy on-axis [20] beam contained within the vacuum laser spot with a halo of high-energy protons with energies $\lesssim 2$ MeV. The spatial distribution of each energy bucket is inset (bottom left-hand corner) and clearly shows the low-energy axial beam (< 0.7 MeV) with the high-energy ring.

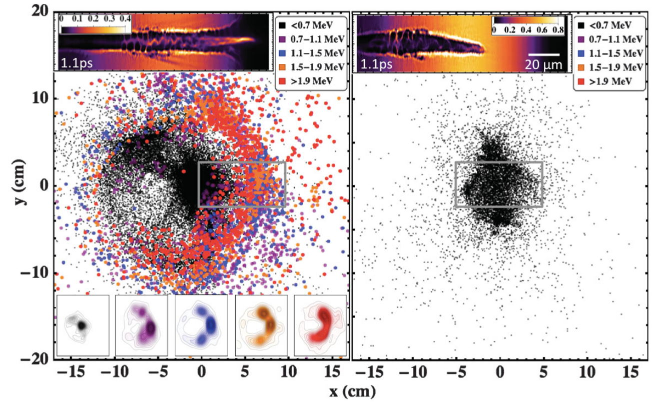

FIG. 4. The spatial distribution of test particles as projected to the plane of the detector for $0.3n_{\mathrm{crit}}$ (left) and $0.6n_{\mathrm{crit}}$ (right). The gray box indicated the region extracted in Fig. 3. Inset below are contour plots of the proton spatial distributions corresponding to the various energy buckets. Inset above are proton density plots taken along the polarization plane for each case. Note that for the $0.3n_{\mathrm{crit}}$ case the cavitation region extends the entire length of the plasma while it only extend halfway through for the $0.6n_{\mathrm{crit}}$ case.

When examining the proton density plot, we observe that at these densities the laser pulse is able to penetrate through the entire plasma. The Z pinch is also clearly seen extending through the plasma. To better illustrate the dynamic process that is occurring, 3D renderings showing the evolution of the electron plasma density, magnetic field lines, and the proton test particles are shown in Fig. 5. Initially, the intense laser pulse undergoes self-focusing and modulation instability in the density up ramp of the plasma region. The ponderomotive force of the pulse drives electron cavitations. Plasma electrons become trapped and accelerated within these cavitations. Because of the slow plasma wave phase velocity and short dephasing length, electrons are easily injected, accelerated, and then stream out of the trapping region of the wakefield. These fast electrons trail behind the laser front, forming an axial fast current. To maintain plasma quasineutrality, a cold electron return current is formed to balance the fast current. The two oppositely signed currents repel one another, forming an axial fast current and a cylindrical-shell cold return current. The on-axis fast current has an average current of 22 kA. This process leads to the generation of a large (~50 MG) azimuthal magnetic field contained within the region. During this process, the mobile ions pinch on axis and an electron-ion pinch is formed with $n_e \approx n_i \approx 0.3n_{\mathrm{crit}}$ and radius of $\sim 1\ \mu$m. This whole process trails the intense laser pulse until it exits the plasma region.

At the exit, the laser pulse ponderomotively expels the ambient electrons from the density ramp. After the intense laser pulse exits the plasma, the fast electron current and large azimuthal magnetic fields begin to flow out, and a situation reminiscent of the magnetic vortex acceleration mechanism occurs. The protons at the interface undergo the same inward pinch as those inside the main plasma region; however, the

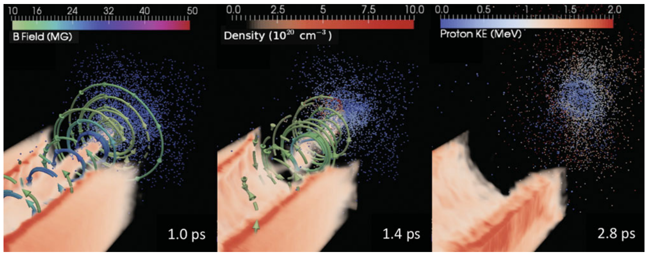

FIG. 5. 3D volumetric renderings of the electron density and azimuthal fields with proton test particles included. The test particles are color coded by their kinetic energy. Note that test particles have a radial energy distribution with lowest energy on axis and the highest off axis. A movie of these simulation results is provided as Supplemental Material [17].

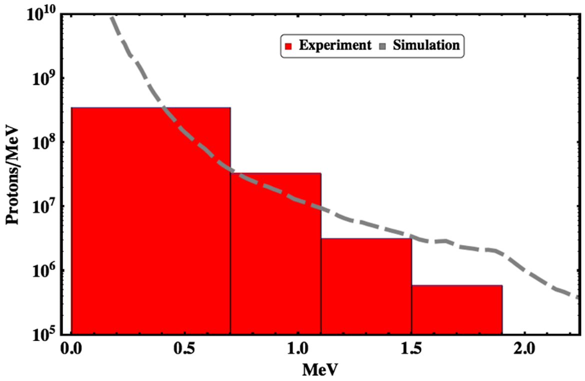

FIG. 6. Plot comparing experimental to simulated proton energy spectrum for $n_e = 0.3 n_{\mathrm{crit}}$. Proton distribution asymmetries, simulated experimental parameters, or sampling statistics with PIC macroparticles may be the cause of discrepancies at higher energies.

magnitude of pinch rapidly drops off due to the drop in density. The fast current eventually leaves the plasma. At this point the magnetic fields begin to dissipate and the protons, no longer confined, explode outward radially. At the same time, they acquire longitudinal momentum from the space-charge fields set up by the escaping fast current. These protons are those observed in the high-energy halo. Additionally, there exist a low-density population of protons outside the ramp. These are accelerated collectively by the fast electrons leaving the plasma region. These protons are the source of low-energy protons on axis. Examining the test particle energy in the final rendering, it can be seen that the proton beam exhibits an energy distribution that is radially dependent, as in the experiments.

Using the test particle results, we directly compared the proton energy spectrum to that observed in the experiments. The results are plotted in Fig. 6. Pit counting of the CR-39 plate was preformed by producing a composite image from a motorized scanning microscope. The pits were then counted using the cell counting algorithm within the image analysis software, ImageJ. In the analysis of the experimental proton energy spectrum, we assumed that the proton distributions were symmetric about the beam axis. Additionally, we subtracted out higher-energy totals from lower-energy bands to prevent double counting. The results show general agreement between experiment and simulations. The simulations do predict higher-energy protons; however, this may be due to proton distribution asymmetries, discrepancies in the simulated experimental conditions, or sampling statistics with PIC macroparticles.

The overall agreement between the experiments, simulations, and theory aids in validating our results. Scaling these results to existing simulation work, we observed much lower ion energies [9,12–16]. This disagreement is directly due to the highly 3D nature of the process. Namely, reducing the process to one transverse dimension constrains the degrees of freedom afforded to the pinch. This was observed when 2D simulations with identical initial conditions to the ones above were preformed [21]. While predicting a lower peak density, these simulations produced a peak proton energy of 13 MeV, much higher than what was observed in experiment and 3D simulations. The momentum that would normally go into the second transverse dimension is instead distributed between the other two dimensions, resulting in a higher overall kinetic energy. It is interesting to note that the 2D simulations were able to produce the same energy for the on-axis beam. This is due to the longitudinal accelerating force produced by the forward directed electrons.

Using a gas foil target, we have observed the transition from TNSA acceleration to magnetic vortex acceleration. In addition, we have discovered a unique signature of magnetic vortex acceleration, namely, the formation of a high-energy halo. This acceleration mechanism is directly controlled by the laser and plasma parameters. By tailoring the plasma peak density, thickness, and gradients, it could be possible to explore regions of higher magnetic fields and produce even higher-energy beams. This target and mechanism provide a potential route to high repetition rate generation of laser-accelerated proton beams.

This work was supported by the Department of Energy and the Naval Research Laboratory Base Program. We would like to acknowledge helpful discussions with B. Hafizi, S. Bulanov, J. Penano, and A. Zingale.

---

[*] Present address: U.S. Naval Research Laboratory, 4555 Overlook Avenue, SW, Washington, D.C. 20375, USA. mike.helle@nrl.navy.mil

[†] Present address: Research Support Instruments, 4325-B Forbes Boulevard, Lanham, Maryland 20706, USA.

[1] A. Macchi, M. Borghesi, and M. Passoni, Rev. Mod. Phys. **85**, 751 (2013).
[2] B. Albright, L. Yin, K. J. Bowers, B. Hegelich, K. Flippo, T. Kwan, and J. Fernandez, Phys. Plasmas **14**, 094502 (2007).
[3] I. Pogorelsky, N. Dover, M. Babzien, A. Bell, A. Dangor, T. Horbury, C. Palmer, M. Polyanskiy, J. Schreiber, S. Schwartz *et al.*, in *Proceedings of the 15th Advanced Accelerator Concepts Workshop* (AIP Publishing, New York, 2012), Vol. 1507, pp. 814–819.
[4] J. Fuchs, P. Antici, E. d'Humières, E. Lefebvre, M. Borghesi, E. Brambrink, C. Cecchetti, M. Kaluza, V. Malka, M. Manclossi *et al.*, Nat. Phys. **2**, 48 (2006).
[5] L. Yin, B. J. Albright, K. J. Bowers, D. Jung, J. C. Fernández, and B. M. Hegelich, Phys. Rev. Lett. **107**, 045003 (2011).
[6] A. Henig, S. Steinke, M. Schnürer, T. Sokollik, R. Hörlein, D. Kiefer, D. Jung, J. Schreiber, B. Hegelich, X. Yan *et al.*, Phys. Rev. Lett. **103**, 245003 (2009).
[7] C. A. Palmer, N. Dover, I. Pogorelsky, M. Babzien, G. Dudnikova, M. Ispiriyan, M. Polyanskiy, J. Schreiber, P. Shkolnikov, V. Yakimenko *et al.*, Phys. Rev. Lett. **106**, 014801 (2011).

[8] D. Haberberger, S. Tochitsky, F. Fiuza, C. Gong, R. A. Fonseca, L. O. Silva, W. B. Mori, and C. Joshi, Nat. Phys. **8**, 95 (2012).

[9] D. F. Gordon, M. H. Helle, D. Kaganovich, A. Ting, and B. Hafizi, in *SPIE Optics + Optoelectronics*, SPIE Proceedings Vol. 9514 (SPIE-International Society for Optics and Photonics, Bellingham, WA, 2013), pp. 951409-1–951409-7.

[10] D. Kaganovich, D. Gordon, M. Helle, and A. Ting, J. Appl. Phys. **116**, 013304 (2014).

[11] D. Kaganovich, M. Helle, D. Gordon, and A. Ting, Appl. Phys. Lett. **97**, 191501 (2010).

[12] S. Bulanov, T. Z. Esirkepov, F. Califano, Y. Kato, T. Liseikina, K. Mima, N. Naumova, K. Nishihara, F. Pegoraro, H. Ruhl *et al.*, J. Exp. Theor. Phys. Lett. **71**, 407 (2000).

[13] L. Willingale, S. P. Mangles, P. M. Nilson, R. J. Clarke, A. E. Dangor, M. C. Kaluza, S. Karsch, K. L. Lancaster, W. B. Mori, J. Schreiber *et al.*, IEEE Trans. Plasma Sci. **36**, 1825 (2008).

[14] T. Nakamura, S. V. Bulanov, T. Z. Esirkepov, and M. Kando, Phys. Rev. Lett. **105**, 135002 (2010).

[15] Y. Sentoku, T. Liseikina, T. Z. Esirkepov, F. Califano, N. Naumova, Y. Ueshima, V. Vshivkov, Y. Kato, K. Mima, K. Nishihara *et al.*, Phys. Rev. E **62**, 7271 (2000).

[16] S. S. Bulanov, V. Y. Bychenkov, V. Chvykov, G. Kalinchenko, D. W. Litzenberg, T. Matsuoka, A. G. Thomas, L. Willingale, V. Yanovsky, K. Krushelnick *et al.*, Phys. Plasmas **17**, 043105 (2010).

[17] See Supplemental Material at http://link.aps.org/supplemental/10.1103/PhysRevLett.117.165001 for further discussion on interferometric measurements of density profiles and animated 3D volumetric rendering of PIC simulation.

[18] F. Séguin, J. Frenje, C. Li, D. Hicks, S. Kurebayashi, J. Rygg, B.-E. Schwartz, R. Petrasso, S. Roberts, J. Soures *et al.*, Rev. Sci. Instrum. **74**, 975 (2003).

[19] D. F. Gordon, IEEE Trans. Plasma Sci. **35**, 1486 (2007).

[20] A slight deviation of the low-energy beam when compared to the vacuum laser axis exists ($< 5°$). We believe that this is possibly due to refraction of the laser beam as it enters the concave surface of the shock at a non-normal angle.

[21] M. Helle, D. Gordon, D. Kaganovich, Y.-H. Chen, and A. Ting, in *SPIE Optics + Optoelectronics*, SPIE Proceedings Vol. 8779 (SPIE-International Society for Optics and Photonics, Bellingham, WA, 2015), pp. 0877902-1–0877902-11.